1

Photoacoustic Imaging for Attenuating Acoustic Media

Habib Ammari[1], Elie Bretin[2], Vincent Jugnon[2], and Abdul Wahab[2]

[1] Department of Mathematics and Applications, Ecole Normale Supérieure, 45
Rue d'Ulm, 75005 Paris, France `habib.ammari@ens.fr`
[2] Centre de Mathématiques Appliquées, CNRS UMR 7641, Ecole Polytechnique,
91128 Palaiseau, France `bretin@cmap.polytechnique.fr,`
`jugnon@cmap.polytechnique.fr, wahab@cmap.polytechnique.fr`

Summary. The aim of this chapter is to consider two challenging problems in
photo-acoustic imaging. We provide algorithms to correct the effects of imposed
boundary conditions and that of attenuation as well. We consider extended optical
sources in an attenuating acoustic background. By testing our measurements against
an appropriate family of functions, we show that we can access the Radon transform
of the initial condition in the acoustic wave equation, and thus recover quantitatively
the absorbing energy density. We also show how to compensate the effect of acoustic
attenuation on image quality by using the stationary phase theorem.

1.1 Introduction

In photo-acoustic imaging, optical energy absorption causes thermo-elastic
expansion of the tissue, which leads to the propagation of a pressure wave.
This signal is measured by transducers distributed on the boundary of the
object, which in turn is used for imaging optical properties of the object. The
major contribution of photo-acoustic imaging is to provide images of optical
contrasts (based on the optical absorption) with the resolution of ultrasound
[33].

If the medium is acoustically homogeneous and has the same acoustic
properties as the free space, then the boundary of the object plays no role and
the optical properties of the medium can be extracted from measurements of
the pressure wave by inverting a spherical Radon transform [23].

In some settings, free space assumptions does not hold. For example, in
brain imaging, the skull plays an important acoustic role, and in small ani-
mal imaging devices, the metallic chamber may have a strong acoustic effect.
In those cases, one has to account for boundary conditions. If a boundary
condition has to be imposed on the pressure field, then an explicit inversion
formula no longer exists. However, using a quite simple duality approach, one

can still reconstruct the optical absorption coefficient. In fact, in the recent works [2, 3], we have investigated quantitative photoacoustic imaging in the case of a bounded medium with imposed boundary conditions. In a further study [1], we proposed a geometric-control approach to deal with the case of limited view measurements. In both cases, we focused on a situation with small optical absorbers in a non-absorbing background and proposed adapted algorithms to locate the absorbers and estimate their absorbed energy.

A second challenging problem in photo-acoustic imaging is to take into account the issue of modelling the acoustic attenuation and its compensation. This subject is addressed in [25, 7, 28, 19, 21, 26, 29, 31]. The reader is in particular referred to [20] for a very nice discussion on the attenuation models and their causality properties.

In this chapter, we propose a new approach to image extended optical sources from photo-acoustic data and to correct the effect of acoustic attenuation. By testing our measurements against an appropriate family of functions, we show that we can access the Radon transform of the initial condition, and thus recover quantitatively any initial condition for the photoacoustic problem. We also show how to compensate the effect of acoustic attenuation on image quality by using the stationary phase theorem. We use a frequency power-law model for the attenuation losses.

The chapter is organized as follows. In Section 1.2 we consider the photo-acoustic imaging problem in free space. We first propose three algorithms to recover the absorbing energy density from limited-view and compare their speeds of convergence. We then present two approaches to correct the effect of acoustic attenuation. We use a power-law model for the attenuation. We test the singular value decomposition approach proposed in [25] and provide a new a technique based on the stationary phase theorem. Section 1.3 is devoted to correct the effect of imposed boundary conditions. By testing our measurements against an appropriate family of functions, we show how to obtain the Radon transform of the initial condition in the acoustic wave equation, and thus recover quantitatively the absorbing energy density. We also show how to compensate the effect of acoustic attenuation on image quality by using again the stationary phase theorem. The chapter ends with a discussion.

1.2 Photo-acoustic imaging in free space

In this section, we first formulate the imaging problem in free space and present a simulation for the reconstruction of the absorbing energy density using the spherical Radon transform. Then, we provide a total variation regularization to find a satisfactory solution of the imaging problem with limited-view data. Finally, we present algorithms for compensating the effect of acoustic attenuation. The main idea is to express the effect of attenuation as a convolution operator. Attenuation correction is then achieved by inverting this operator. Two strategies are used for such deconvolution. The first one is based

on the singular value decomposition of the operator and the second one uses its asymptotic expansion based on the stationary phase theorem. We compare the performances of the two approaches.

1.2.1 Mathematical formulation

We consider the wave equation in $\mathbb{R}^d$,

$$\frac{1}{c_0^2} \frac{\partial^2 p}{\partial t^2}(x,t) - \Delta p(x,t) = 0 \quad \text{in } \mathbb{R}^d \times (0,T),$$

with

$$p(x,0) = p_0 \quad \text{and} \quad \frac{\partial p}{\partial t}(x,0) = 0.$$

Here c_0 is the phase velocity in a non-attenuating medium.

Assume that the support of p_0, the absorbing energy density, is contained in a bounded set Ω of $\mathbb{R}^d$. Our objective in this part is to reconstruct p_0 from the measurements $g(y,t) = p(y,t)$ on $\partial\Omega \times (0,T)$, where $\partial\Omega$ denotes the boundary of Ω.

The problem of reconstructing p_0 is related to the inversion of the spherical Radon transform given by

$$\mathcal{R}_\Omega[f](y,r) = \int_S r f(y + r\xi) \, d\sigma(\xi), \quad (y,r) \in \partial\Omega \times \mathbb{R}^+,$$

where S denotes the unit sphere. It is known that in dimension 2, Kirchhoff's formula implies that [14]

$$\begin{cases} p(y,t) = \dfrac{1}{2\pi} \partial_t \displaystyle\int_0^t \dfrac{\mathcal{R}_\Omega[p_0](y,c_0 r)}{\sqrt{t^2 - r^2}} \, dr, \\[4mm] \mathcal{R}_\Omega[p_0](y,r) = 4r \displaystyle\int_0^r \dfrac{p(y,t/c_0)}{\sqrt{r^2 - t^2}} \, dt. \end{cases}$$

Let the operator $\mathcal{W}$ be defined by

$$\mathcal{W}[g](y,r) = 4r \int_0^r \frac{g(y,t/c_0)}{\sqrt{r^2 - t^2}} \, dt \quad \text{for all } g : \partial\Omega \times \mathbb{R}^+ \to \mathbb{R}. \tag{1.1}$$

Then, it follows that

$$\mathcal{R}_\Omega[p_0](y,r) = \mathcal{W}[p](y,r). \tag{1.2}$$

In recent works, a large class of inversion retroprojection formulae for the spherical Radon transform have been obtained in even and odd dimensions when Ω is a ball, see for instance [14, 24, 13, 27]. In dimension 2 when Ω is the unit disk, it turns out that

$$p_0(x) = \frac{1}{(4\pi^2)} \int_{\partial\Omega} \int_0^2 \left[\frac{d^2}{dr^2} \mathcal{R}_\Omega[p_0](y,r) \right] \ln |r^2 - (y-x)^2| \, dr \, d\sigma(y). \quad (1.3)$$

This formula can be rewritten as follows:

$$p_0(x) = \frac{1}{4\pi^2} \mathcal{R}_\Omega^* \mathcal{B} \mathcal{R}_\Omega[p_0](x), \quad (1.4)$$

where $\mathcal{R}_\Omega^*$ is the adjoint of $\mathcal{R}_\Omega$,

$$\mathcal{R}_\Omega^*[g](x) = \int_{\partial\Omega} g(y, |y-x|) \, d\sigma(y),$$

and $\mathcal{B}$ is defined by

$$\mathcal{B}[g](x,t) = \int_0^2 \frac{d^2 g}{dr^2}(y,r) \ln(|r^2 - t^2|) \, dr$$

for $g : \Omega \times \mathbb{R}^+ \to \mathbb{R}$.

In Figure 1.1, we give a numerical illustration for the reconstruction of p_0 using the spherical Radon transform. We adopt the same approach as in [13] for the discretization of formulae (1.1) and (1.3). Note that in the numerical examples presented in this section, N_θ denotes the number of equally spaced angles on $\partial\Omega$, the pressure signals are uniformly sampled at N time steps, and the phantom (the initial pressure distribution p_0) is sampled on a uniform Cartesian grid with $N_R \times N_R$ points.

1.2.2 Limited-view data

In many situations, we have only at our disposal data on $\Gamma \times (0,T)$, where $\Gamma \subset \partial\Omega$. As illustrated in Figure 1.2, restricting the integration in formula (1.3) to Γ as follows:

$$p_0(x) \simeq \frac{1}{(4\pi^2)} \int_\Gamma \int_0^2 \left[\frac{d^2}{dr^2} \mathcal{R}_\Omega[p_0](y,r) \right] \ln |r^2 - (y-x)^2| \, dr \, d\sigma(y), \quad (1.5)$$

is not stable enough to give a correct reconstruction of p_0.

The inverse problem becomes severely ill-posed and needs to be regularized (see for instance [34, 15]). We apply here a Tikhonov regularization with a total variation term, which is well adapted to the reconstruction of smooth solutions with front discontinuities. We then introduce the function $p_{0,\eta}$ as the minimizer of

$$J[f] = \frac{1}{2} \| Q \left[\mathcal{R}_\Omega[f] - g \right] \|_{L^2(\partial\Omega \times (0,2))}^2 + \eta \| \nabla f \|_{L^1(\Omega)},$$

where Q is a positive weight operator.

Direct computation of $p_{0,\eta}$ can be complicated as the TV term is not smooth (not of class $\mathcal{C}^1$). Here, we obtain an approximation of $p_{0,\eta}$ via an iterative shrinkage-thresholding algorithm [12, 10]. This algorithm can be viewed as a split, gradient-descent, iterative scheme:
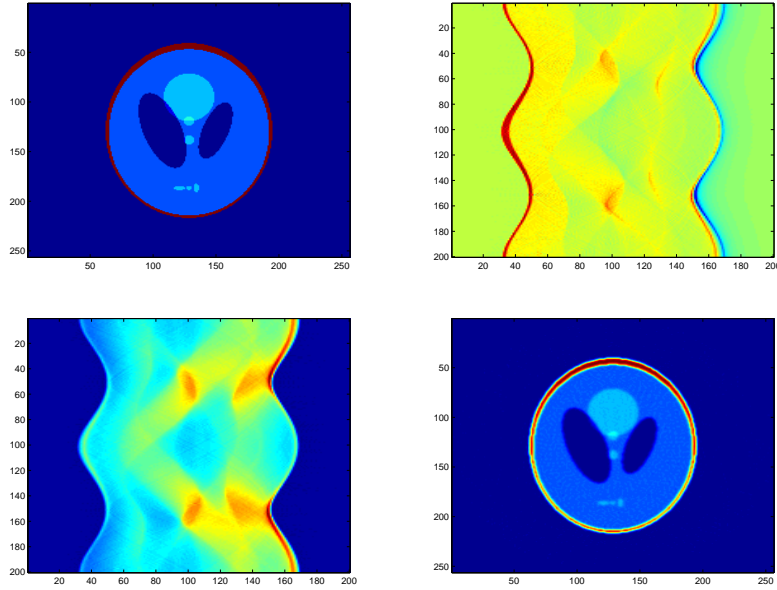
Fig. 1.1. Numerical inversion using (1.3) with $N = 256$, $N_R = 200$ and $N_\theta = 200$. Top left: p_0 ; Top right: $p(y,t)$ with $(y,t) \in \partial\Omega \times (0,2)$; Bottom left: $\mathcal{R}_\Omega[p_0](y,t)$ with $(y,t) \in \partial\Omega \times (0,2)$; Bottom right: $\frac{1}{4\pi^2} \mathcal{R}_\Omega^* \mathcal{B} \mathcal{R}_\Omega[p_0]$.
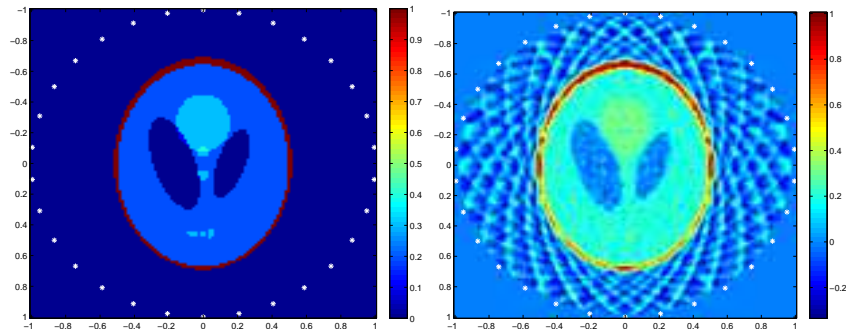

Fig. 1.2. Numerical inversion with truncated (1.3) formula with $N = 128$, $N_R = 128$, and $N_\theta = 30$. Left: p_0; Right: $\frac{1}{4\pi^2} \mathcal{R}_\Omega^* \mathcal{B} \mathcal{R}_\Omega[p_0]$.

- Data g, initial solution $f_0 = 0$;
- *(1) Data link step:* $f_{k+1/2} = f_k - \gamma \mathcal{R}_\Omega^* Q^* Q \left[\mathcal{R}_\Omega[f_k] - g \right]$;
- *(2) Regularization step:* $f_k = T_{\gamma\eta}[f_{k+1/2}]$,

where γ is a virtual descent time step and the operator T_η is given by

$$T_\eta[y] = \arg \min_x \left\{ \frac{1}{2} \|y - x\|_{L^2}^2 + \eta \|\nabla x\|_{L^1} \right\}.$$

Note that T_η defines a proximal point method. One advantage of the algorithm is to minimize implicitly the TV term using the duality algorithm of Chambolle [8]. This algorithm converges [12, 10] under the assumption $\gamma \|\mathcal{R}_\Omega^* Q^* Q \mathcal{R}_\Omega\| \leq 1$, but its rate of convergence is known to be slow. Thus, in order to accelerate the convergence rate, we will also consider the variant algorithm of Beck and Teboulle [6] defined as

- Data g, initial set: $f_0 = x_0 = 0$, $t_1 = 1$;
- *(1)* $x_k = T_{\gamma\eta} \left(f_k - \gamma \mathcal{R}_\Omega^* Q^* Q \left[\mathcal{R}_\Omega[f_k] - g \right] \right)$;
- *(2)* $f_{k+1} = x_k + \frac{t_k - 1}{t_{k+1}} (x_k - x_{k-1})$ with $t_{k+1} + \frac{1 + \sqrt{1 + 4t_k^2}}{2}$.

The standard choice of Q is the identity, Id, and then it is easy to see that $\|R_\Omega R_\Omega^*\| \simeq 2\pi$. It will also be interesting to use $Q = \frac{1}{2\pi} \mathcal{B}^{1/2}$, which is well defined since $\mathcal{B}$ is symmetric and positive. In this case, $\mathcal{R}_\Omega^* Q^* Q \simeq \mathcal{R}_\Omega^{-1}$ and we can hope to improve the convergence rate of the regularized algorithm.

We compare three algorithms of this kind in Figure 1.3. The first and the second one correspond to the simplest algorithm with respectively $Q = $ Id and $Q = \frac{1}{2\pi} \mathcal{B}^{1/2}$. The last method uses the variant of Beck and Teboulle with $Q = \frac{1}{2\pi} \mathcal{B}^{1/2}$. The speed of convergence of each of these algorithms is plotted in Figure 1.3. Clearly, the third method is the best and after 30 iterations, a very good approximation of p_0 is reconstructed.

Two limited-angle experiments are presented in Figure 1.4 using the third algorithm.

1.2.3 Compensation of the effect of acoustic attenuation

Our aim in this section is to compensate for the effect of acoustic attenuation. The pressures $p(x, t)$ and $p_a(x, t)$ are respectively solutions of the following wave equations:

$$\frac{1}{c_0^2} \frac{\partial^2 p}{\partial t^2}(x, t) - \Delta p(x, t) = \frac{1}{c_0^2} \delta'_{t=0} p_0(x),$$

and

$$\frac{1}{c_0^2} \frac{\partial^2 p_a}{\partial t^2}(x, t) - \Delta p_a(x, t) - L(t) * p_a(x, t) = \frac{1}{c_0^2} \delta'_{t=0} p_0(x),$$
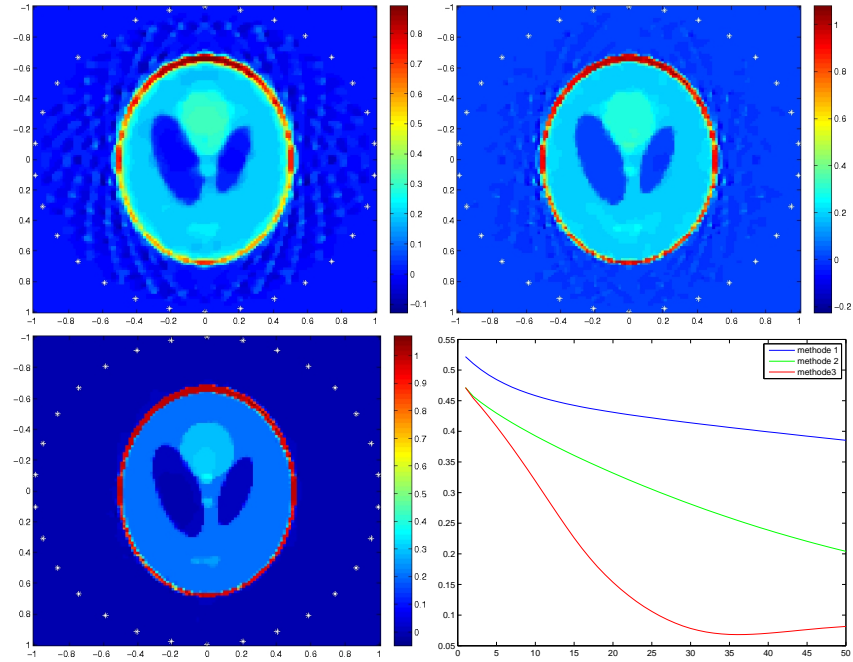
where L is defined by

Fig. 1.3. Iterative shrinkage-thresholding solution after 30 iterations with $\eta = 0.01$, $N = 128$, $N_R = 128$, and $N_\theta = 30$. Top left: simplest algorithm with $Q = \mathrm{Id}$ and $\mu = 1/(2\pi)$; Top right: simplest algorithm with $Q = \frac{1}{2\pi}\mathcal{B}^{1/2}$ and $\mu = 0.5$; Bottom left: Beck and Teboulle variant with $Q = \frac{1}{2\pi}\mathcal{B}^{1/2}$ and $\mu = 0.5$; Bottom right: error $k \to \|f_k - p_0\|_\infty$ for each of the previous situations.
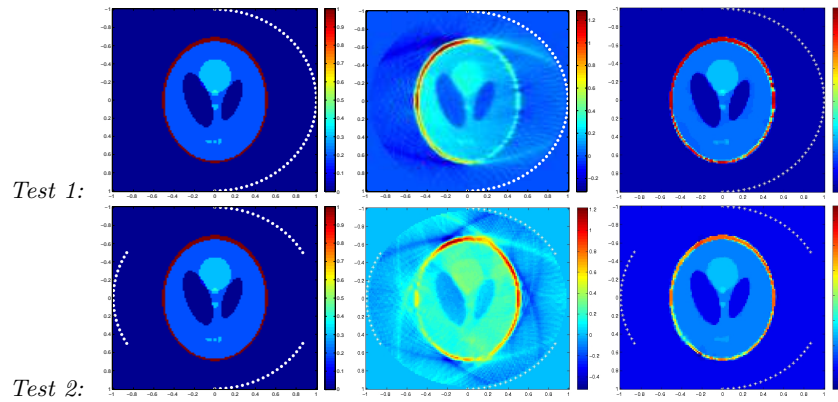

Fig. 1.4. Case of limited angle with Beck and Teboulle iterative shrinkage-thresholding after 50 iterations, with parameters equal to $\eta = 0.01$, $N = 128$, $N_R = 128$, $N_\theta = 64$ and $Q = \frac{1}{2\pi}\mathcal{B}^{1/2}$. Left: p_0; Center: $\frac{1}{4\pi^2}\mathcal{R}_\Omega^* \mathcal{B}\mathcal{R}_\Omega[p_0]$; Right: f_{50}.

$$L(t) = \frac{1}{\sqrt{2\pi}} \int_{\mathbb{R}} \left(K^2(\omega) - \frac{\omega^2}{c_0^2} \right) e^{i\omega t} d\omega. \tag{1.6}$$

Many models exist for $K(\omega)$. Here we use the power-law model. Then $K(\omega)$ is the complex wave number, defined by

$$K(\omega) = \frac{\omega}{c(\omega)} + ia|\omega|^\zeta, \tag{1.7}$$

where ω is the frequency, $c(\omega)$ is the frequency dependent phase velocity and $1 \leq \zeta \leq 2$ is the power of the attenuation coefficient. See [30]. A common model, known as the thermo-viscous model, is given by $K(\omega) = \frac{\omega}{c_0\sqrt{1-ia\omega c_0}}$ and corresponds approximately to $\zeta = 2$ with $c(\omega) = c_0$.

Our strategy is now to:

- Estimate $p(y,t)$ from $p_a(y,t)$ for all $(y,t) \in \partial\Omega \times \mathbb{R}^+$.
- Apply the inverse formula for the spherical Radon transform to reconstruct p_0 from the non-attenuated data.

A natural definition of an attenuated spherical Radon transform $\mathcal{R}_{a,\Omega}$ is

$$\mathcal{R}_{a,\Omega}[p_0] = \mathcal{W}[p_a]. \tag{1.8}$$

1.2.4 Relationship between p and p_a

Recall that the Fourier transforms of p and p_a satisfy

$$\left(\Delta + (\frac{\omega}{c_0})^2 \right) \hat{p}(x,\omega) = \frac{i\omega}{\sqrt{2\pi}c_0^2} p_0(x) \quad \text{and} \quad \left(\Delta + K(\omega)^2 \right) \hat{p_a}(x,\omega) = \frac{i\omega}{\sqrt{2\pi}c_0^2} p_0(x),$$

which implies that

$$\hat{p}(x, c_0 K(\omega)) = \frac{c_0 K(\omega)}{\omega} \hat{p_a}(x,\omega).$$

The issue is to estimate p from p_a using the relationship $p_a = \mathcal{L}[p]$, where $\mathcal{L}$ is defined by

$$\mathcal{L}[\phi](s) = \frac{1}{2\pi} \int_{\mathbb{R}} \frac{\omega}{c_0 K(\omega)} e^{-i\omega s} \int_0^\infty \phi(t) e^{ic_0 K(\omega)t} \, dt \, d\omega.$$

The main difficulty is that $\mathcal{L}$ is not well conditioned. We will compare two approaches. The first one uses a regularized inverse of $\mathcal{L}$ via a singular value decomposition (SVD), which has been recently introduced in [25]. The second one is based on the asymptotic behavior of $\mathcal{L}$ as the attenuation coefficient a tends to zero.

Figure 1.5 gives some numerical illustrations of the inversion of the attenuated spherical Radon transform without a correction of the attenuation effect, where a thermo-viscous attenuation model is used with $c_0 = 1$.
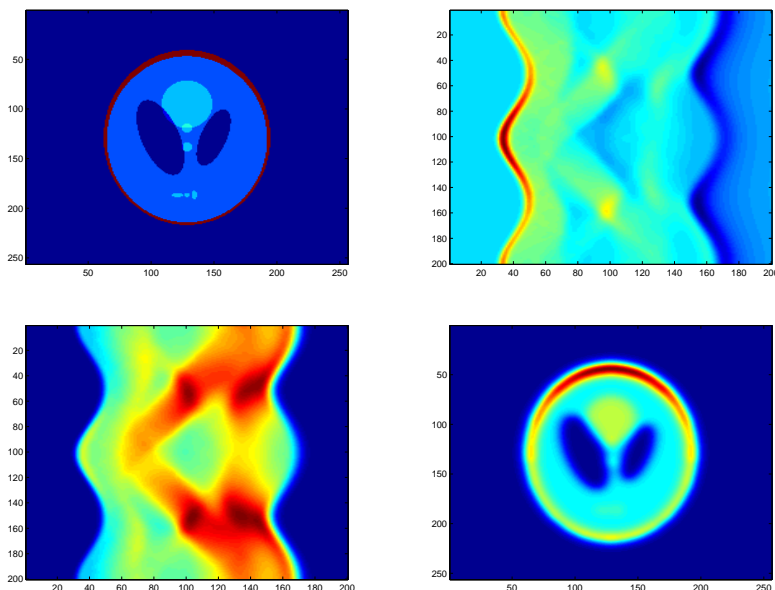
Fig. 1.5. Numerical inversion of attenuated wave equation with $K(\omega) = \frac{\omega}{c_0} + ia\omega^2/2$ and $a = 0.001$. Here $N = 256$, $N_R = 200$ and $N_\theta = 200$. Top left: p_0; Top right: $p_a(y,t)$ with $(y,t) \in \partial\Omega \times (0,2)$; Bottom left: $\mathcal{W}p_a(y,t)$ with $(y,t) \in \partial\Omega \times (0,2)$; Bottom right: $\frac{1}{4\pi^2}\mathcal{R}_\Omega^* \mathcal{B}\left(\mathcal{W}[p_a](y,t)\right)$.

1.2.5 A SVD approach

La Rivière, Zhang, and Anastasio have recently proposed in [25] to use a regularized inverse of the operator $\mathcal{L}$ obtained by a standard SVD approach:

$$\mathcal{L}[\phi] = \sum_l \sigma_l \langle \phi, \tilde{\psi}_l \rangle \psi_l,$$

where $(\tilde{\psi}_l)$ and (ψ_l) are two orthonormal bases of $L^2(0,T)$ and σ_l are positives eigenvalues such that

$$\begin{cases} \mathcal{L}^*[\phi] &= \sum_l \sigma_l \langle \phi, \psi_l \rangle \tilde{\psi}_l, \\ \mathcal{L}^*\mathcal{L}[\phi] &= \sum_l \sigma_l^2 \langle \phi, \tilde{\psi}_l \rangle \tilde{\psi}_l, \\ \mathcal{L}\mathcal{L}^*[\phi] &= \sum_l \sigma_l^2 \langle \phi, \psi_l \rangle \psi_l. \end{cases}$$

An ϵ-approximation inverse of $\mathcal{L}$ is then given by

$$\mathcal{L}_{1,\epsilon}^{-1}[\phi] = \sum_l \frac{\sigma_l}{\sigma_l^2 + \epsilon^2} \langle \phi, \psi_l \rangle \tilde{\psi}_l,$$

where $\epsilon > 0$.

In Figure 1.6 we present some numerical inversions of the thermo-viscous wave equation with $a = 0.0005$ and $a = 0.0025$. We first obtain the ideal measurements from the attenuated ones and then apply the inverse formula for the spherical Radon transform to reconstruct p_0 from the ideal data. We take ϵ respectively equal to 0.01, 0.001 and 0.0001. The operator $\mathcal{L}$ is discretized to obtain an $N_R \times N_R$ matrix to which we apply an SVD decomposition. A regularization of the SVD allows us to construct $\mathcal{L}_{1,\epsilon}^{-1}$.

As expected, this algorithm corrects a part of the attenuation effect but is unstable when ϵ tends to zero.
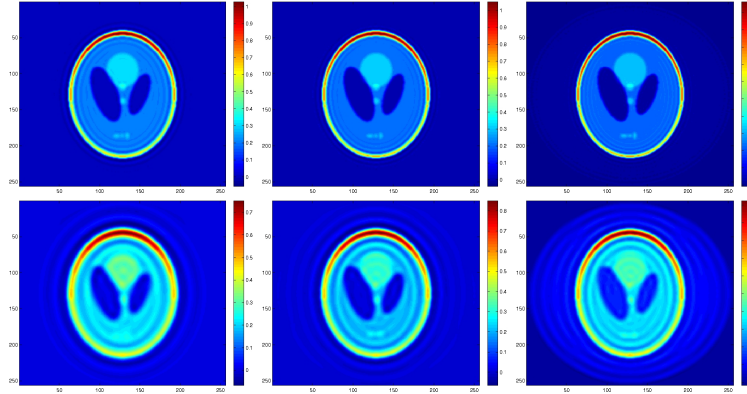

Fig. 1.6. Compensation of acoustic attenuation with SVD regularization: $N = 256$, $N_R = 200$ and $N_\theta = 200$. First line: $a = 0.0005$; second line: $a = 0.0025$. Left to right: using $\mathcal{L}_{1,\epsilon}^{-1}$ respectively with $\epsilon = 0.01$, $\epsilon = 0.001$ and $\epsilon = 0.0001$.

1.2.6 Asymptotics of $\mathcal{L}$

In physical situations, the coefficient of attenuation a is very small. We will take into account this phenomenon and introduce an approximation of $\mathcal{L}$ and $\mathcal{L}^{-1}$ as a goes to zero:

$$\mathcal{L}_k[\phi] = \mathcal{L}[\phi] + o(a^{k+1}) \quad \text{and} \quad \mathcal{L}_{2,k}^{-1}[\phi] = \mathcal{L}^{-1}[\phi] + o(a^{k+1}),$$

where k represents an order of approximation.

Thermo-viscous case: $K(\omega) = \frac{\omega}{c_0} + ia\omega^2/2$

Let us consider in this section the attenuation model $K(\omega) = \frac{\omega}{c_0} + ia\omega^2/2$ at low frequencies $\omega \ll \frac{1}{a}$, such that

$$\frac{1}{1 + iac_0\omega/2} \simeq 1 - i\frac{ac_0}{2}\omega.$$

The operator $\mathcal{L}$ is approximated as follows

$$\mathcal{L}[\phi](s) \simeq \frac{1}{2\pi}\int_0^\infty \phi(t)\int_{\mathbb{R}}\left(1 - i\frac{ac_0}{2}\omega\right)e^{-\frac{1}{2}c_0a\omega^2 t}e^{i\omega(t-s)}\,d\omega\,dt.$$

Since

$$\frac{1}{\sqrt{2\pi}}\int_{\mathbb{R}}e^{-\frac{1}{2}c_0a\omega^2 t}e^{i\omega(t-s)}d\omega = \frac{1}{\sqrt{c_0at}}e^{-\frac{1}{2}\frac{(s-t)^2}{c_0at}},$$

and

$$\frac{1}{\sqrt{2\pi}}\int_{\mathbb{R}}\frac{-iac_0\omega}{2}e^{-\frac{1}{2}c_0a\omega^2 t}e^{i\omega(t-s)}d\omega = \frac{ac_0}{2}\partial_s\left(\frac{1}{\sqrt{c_0at}}e^{-\frac{1}{2}\frac{(s-t)^2}{c_0at}}\right),$$

it follows that

$$\mathcal{L}[\phi] \simeq \left(1 + \frac{ac_0}{2}\partial_s\right)\left(\frac{1}{\sqrt{2\pi}}\int_0^{+\infty}\phi(t)\frac{1}{\sqrt{c_0at}}e^{-\frac{1}{2}\frac{(s-t)^2}{c_0at}}\,dt\right).$$

We then investigate the asymptotic behavior of $\tilde{\mathcal{L}}$ defined by

$$\tilde{\mathcal{L}}[\phi] = \frac{1}{\sqrt{2\pi}}\int_0^{+\infty}\phi(t)\frac{1}{\sqrt{c_0at}}e^{-\frac{1}{2}\frac{(s-t)^2}{c_0at}}\,dt. \tag{1.9}$$

Since the phase in (1.9) is quadratic and a is small, by the stationary phase theorem we can prove that

$$\tilde{\mathcal{L}}[\phi](s) = \sum_{i=0}^k \frac{(c_0a)^i}{2^i i!}D_i[\phi](s) + o(a^k), \tag{1.10}$$

where the differential operators D_i satisfy $D_i[\phi](s) = (t^i\phi(t))^{(2i)}(s)$. See Appendix A.2. We can also deduce the following approximation of order k of $\tilde{\mathcal{L}}^{-1}$

$$\tilde{\mathcal{L}}_k^{-1}[\psi] = \sum_{j=0}^k a^j\psi_{k,j}, \tag{1.11}$$

where $\psi_{k,j}$ are defined recursively by

$$\psi_{k,0} = \psi \quad \text{and} \quad \psi_{k,j} = -\sum_{i=1}^j \frac{1}{i!}D_i[\psi_{k,j-i}], \text{ for all } j \leq k.$$

Finally, we define

$$\mathcal{L}_k = \left(1 + \frac{ac_0}{2}\partial_s\right)\tilde{\mathcal{L}}_k \quad \text{and} \quad \mathcal{L}_{2,k}^{-1} = \tilde{\mathcal{L}}_k^{-1}\left(1 + \frac{ac_0}{2}\partial_t\right)^{-1}. \tag{1.12}$$

We plot in Figure 1.6 some numerical reconstructions of p_0 using a thermo-viscous wave equation with $a = 0.0005$ and $a = 0.0025$. We take the value of k respectively equal to $k = 0$, $k = 1$ and $k = 8$. These reconstructions seem to be as good as those obtained by the SVD regularization approach. Moreover, this new algorithm has better stability properties.
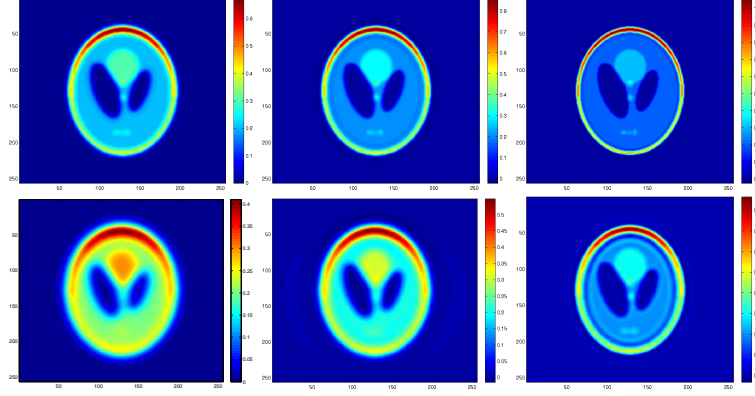

Fig. 1.7. Compensation of acoustic attenuation with formula (1.12): $N = 256$, $N_R = 200$ and $N_\theta = 200$. First line: $a = 0.0005$; second line: $a = 0.0025$. Left: $\tilde{\mathcal{L}}_k^{-1}$ with $k = 0$; Center: $\tilde{\mathcal{L}}_k^{-1}$ with $k = 1$; Right: $\tilde{\mathcal{L}}_k^{-1}$ with $k = 8$.

General case: $K(\omega) = \omega + ia|\omega|^\zeta$ with $1 \leq \zeta < 2$

We now consider the attenuation model $K(\omega) = \frac{\omega}{c_0} + ia|\omega|^\zeta$ with $1 \leq \zeta < 2$. We first note that this model is not causal but can be changed to a causal one [20, 9]. However, since our main purpose here is to give insights for the compensation of the effect of attenuation on image reconstruction, we work with this quite general model because of its simplicity. As before, the problem can be reduced to the approximation of the operator $\tilde{\mathcal{L}}$ defined by

$$\tilde{\mathcal{L}}[\phi](s) = \int_0^\infty \phi(t) \int_{\mathbb{R}} e^{i\omega(t-s)} e^{-|\omega|^\zeta c_0 at} \, d\omega dt.$$

It is also interesting to see that its adjoint $\tilde{\mathcal{L}}^*$ satisfies

$$\tilde{\mathcal{L}}^*[\phi](s) = \int_0^\infty \phi(t) \int_{\mathbb{R}} e^{i\omega(s-t)} e^{-|\omega|^\zeta c_0 as} \, d\omega dt.$$

Suppose for the moment that $\zeta = 1$, and working with the adjoint operator $\mathcal{L}^*$, we see that

$$\tilde{\mathcal{L}}^*[\phi](s) = \frac{1}{\pi} \int_0^\infty \frac{c_0 a s}{(c_0 a s)^2 + (s-t)^2} \phi(t) dt.$$

Invoking the dominated convergence theorem, we have

$$\lim_{a \to 0} \tilde{\mathcal{L}}^*[\phi](s) = \lim_{a \to 0} \frac{1}{\pi} \int_{-\frac{1}{ac_0}}^\infty \frac{1}{1+y^2} \phi(s + c_0 a y s) dy = \frac{1}{\pi} \int_{-\infty}^\infty \frac{1}{1+y^2} \phi(s) dy = \phi(s).$$

More precisely, introducing the fractional Laplacian $\Delta^{1/2}$ as follows

$$\Delta^{1/2}\phi(s) = \frac{1}{\pi} \, \text{p.v.} \int_{-\infty}^{+\infty} \frac{\phi(t) - \phi(s)}{(t-s)^2} \, dt,$$

where p.v. stands for the Cauchy principal value, we get

$$
\begin{aligned}
\frac{1}{a}\left(\tilde{\mathcal{L}}^*[\phi](s) - \phi(s)\right) &= \frac{1}{a} \int_{-\infty}^\infty \frac{1}{\pi c_0 a s} \frac{1}{1 + \left(\frac{s-t}{c_0 a s}\right)^2} \left(\phi(t) - \phi(s)\right) dt \\
&= \int_{-\infty}^\infty \frac{1}{\pi} \frac{c_0 s}{(c_0 a s)^2 + (s-t)^2} \left(\phi(t) - \phi(s)\right) dt \\
&= \lim_{\epsilon \to 0} \int_{\mathbb{R} \backslash [s-\epsilon, s+\epsilon]} \frac{1}{\pi} \frac{c_0 s}{(c_0 a s)^2 + (s-t)^2} \left(\phi(t) - \phi(s)\right) dt \\
&\to \lim_{\epsilon \to 0} \int_{\mathbb{R} \backslash [s-\epsilon, s+\epsilon]} \frac{1}{\pi} \frac{c_0 s}{(s-t)^2} \left(\phi(t) - \phi(s)\right) dt \\
&= c_0 s \Delta^{1/2} \phi(s),
\end{aligned}
$$

as a tends to zero. We therefore deduce that

$$\tilde{\mathcal{L}}^*[\phi](s) = \phi(s) + c_0 a s \Delta^{1/2}\phi(s) + o(a) \quad \text{and} \quad \tilde{\mathcal{L}}^*[\phi](s) = \phi(s) + c_0 a \Delta^{1/2}\left(s\phi(s)\right) + o(a).$$

Applying exactly the same argument for $1 < \zeta < 2$, we obtain that

$$\mathcal{L}[\phi](s) = \phi(s) + C c_0 a \Delta^{\zeta/2}(s\phi(s)) + o(a),$$

where C is a constant, depending only on ζ and $\Delta^{\zeta/2}$, defined by

$$\Delta^{\zeta/2}\phi(s) = \frac{1}{\pi} \, \text{p.v.} \int_{-\infty}^{+\infty} \frac{\phi(t) - \phi(s)}{(t-s)^{1+\zeta}} \, dt.$$

1.2.7 Iterative shrinkage-thresholding algorithm with correction of attenuation

The previous correction of attenuation is not so efficient for a large attenuation coefficient a. In this case, to improve the reconstruction, we may use again a Tikhonov regularization. Let $\mathcal{R}^{-1}_{\Omega, a, k}$ be an approximate inverse of the attenuated spherical Radon transform $\mathcal{R}_{\Omega, a}$:

$$\mathcal{R}^{-1}_{\Omega, a, k} = \mathcal{R}_{\Omega^{-1}} \mathcal{W} \mathcal{L}^{-1}_{2,k} \mathcal{W}^{-1}.$$

Although its convergence is not clear, we will now consider the following iterative shrinkage-thresholding algorithm:

- Data g, initial set: $f_0 = x_0 = 0$, $t_1 = 1$;
- (1) $x_j = T_{\gamma\eta}\left(f_j - \gamma\mathcal{R}_{\Omega,a,k}^{-1}\left(\mathcal{R}_{\Omega,a}f_j - g\right)\right)$;
- (2) $f_{j+1} = x_j + \frac{t_j - 1}{t_{j+1}}\left(x_j - x_{j-1}\right)$ with $t_{j+1} + \frac{1+\sqrt{1+4t_j^2}}{2}$.

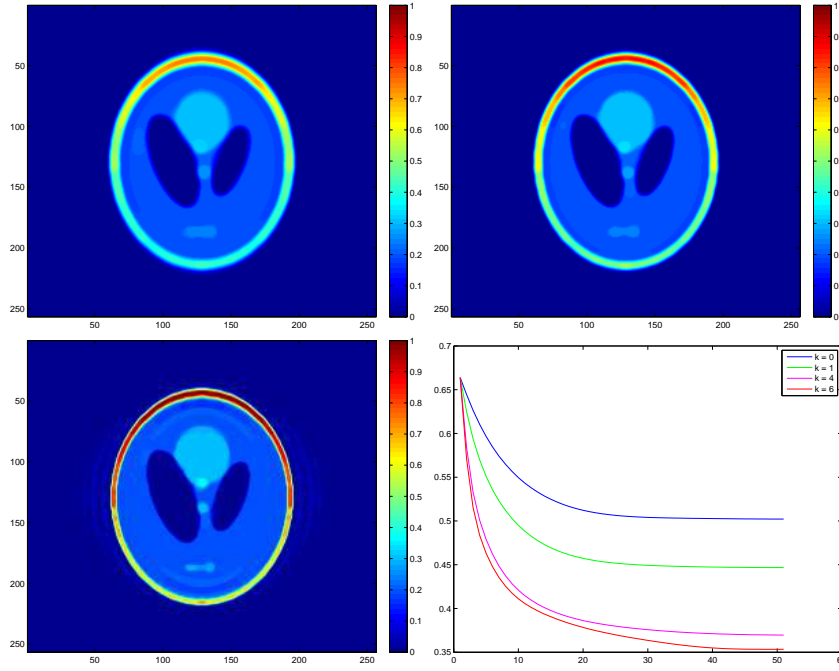Figure 1.8 shows the efficiency of this algorithm.

Fig. 1.8. Numerical results using iterative shrinkage-thresholding algorithm with $\eta = 0.001$ and $a = 0.0025$. Left up: f_{50} with $k = 0$; Top right: f_{50} with $k = 1$; Bottom left: f_{50} with $k = 6$; Bottom right: error $j \to \|f_j - p_0\|$ for different values of k.

1.3 Photo-acoustic imaging with imposed boundary conditions

In this section, we consider the case where a boundary condition has to be imposed on the pressure field. We first formulate the photo-acoustic imaging problem in a bounded domain before reviewing the reconstruction procedures. We refer the reader to [32] where the half-space problem has been considered. We then introduce a new algorithm which reduces the reconstruction problem

to the inversion of a Radon transform. This procedure is particularly well-suited for extended absorbers. Finally, we discuss the issue of correcting the attenuation effect and propose an algorithm analogous to the one described in the previous section.

1.3.1 Mathematical formulation

Let Ω be a bounded domain. We consider the wave equation in the domain Ω:

$$\begin{cases} \dfrac{1}{c_0^2}\dfrac{\partial^2 p}{\partial t^2}(x,t) - \Delta p(x,t) = 0 & \text{in } \Omega \times (0,T), \\ p(x,0) = p_0(x) & \text{in } \Omega, \\ \dfrac{\partial p}{\partial t}(x,0) = 0 & \text{in } \Omega, \end{cases} \tag{1.1}$$

with the Dirichlet (resp. the Neumann) imposed boundary conditions:

$$p(x,t) = 0 \qquad \left(\text{resp. } \frac{\partial p}{\partial \nu}(x,t) = 0\right) \qquad \text{on } \partial\Omega \times (0,T). \tag{1.2}$$

Our objective in the next subsection is to reconstruct $p_0(x)$ from the measurements of $\dfrac{\partial p}{\partial \nu}(x,t)$ (resp. $p(x,t)$) on the boundary $\partial\Omega \times (0,T)$.

1.3.2 Inversion algorithms

Consider probe functions satisfying

$$\begin{cases} \dfrac{1}{c_0^2}\dfrac{\partial^2 v}{\partial t^2}(x,t) - \Delta v(x,t) = 0 & \text{in } \Omega \times (0,T), \\ v(x,T) = 0 & \text{in } \Omega, \\ \dfrac{\partial v}{\partial t}(x,T) = 0 & \text{in } \Omega. \end{cases} \tag{1.3}$$

Multiplying (1.1) by v and integrating by parts yields (in the case of Dirichlet boundary conditions):

$$\int_0^T \int_{\partial\Omega} \frac{\partial p}{\partial \nu}(x,t)v(x,t)d\sigma(x)dt = \int_\Omega p_0(x)\frac{\partial v}{\partial t}(x,0)dx. \tag{1.4}$$

Choosing a probe function v with proper initial time derivative allows us to infer information on p_0 (right-hand side in (1.4)) from our boundary measurements (left-hand side in (1.4)).

In [2], considering a full view setting, we used a 2-parameter travelling plane wave given by

$$v_{\tau,\theta}^{(1)}(x,t) = \delta\left(\frac{x \cdot \theta}{c_0} + t - \tau\right), \tag{1.5}$$

and we determined the inclusions' characteristic functions by varying (θ, τ). We also used in three dimensions the spherical waves given by

$$w_{\tau,y}(x,t) = \frac{\delta\left(t + \tau - \frac{|x-y|}{c_0}\right)}{4\pi|x-y|}, \tag{1.6}$$

for $y \in \mathbb{R}^3 \setminus \Omega$, to probe the medium.

In [1], we assumed that measurements are only made on a part of the boundary $\Gamma \subset \partial\Omega$. Using geometric control, we could choose the form of $\frac{\partial v}{\partial t}(x,0)$ and design a probe function v satisfying (1.3) together with

$$v(x,t) = 0 \qquad \text{on } \partial\Omega \setminus \bar{\Gamma},$$

so that we had

$$\int_0^T \int_\Gamma \frac{\partial p}{\partial \nu}(x,t)v(x,t)d\sigma(x)dt = \int_\Omega p_0(x)\frac{\partial v}{\partial t}(x,0)dx. \tag{1.7}$$

Varying our choice of $\frac{\partial v}{\partial t}(x,0)$, we could adapt classical imaging algorithms (MUSIC, back-propagation, Kirchhoff migration, arrival-time) to the case of limited view data.

Now simply consider the 2-parameter family of probe functions:

$$v_{\tau,\theta}^{(2)}(x,t) = 1 - H\left(\frac{x \cdot \theta}{c_0} + t - \tau\right), \tag{1.8}$$

where H is the Heaviside function. The probe function $v_{\tau,\theta}^{(2)}(x,t)$ is an incoming plane wavefront. Its equivalent, still denoted by $v_{\tau,\theta}^{(2)}$, in the limited-view setting satisfies the initial conditions

$$v_{\tau,\theta}^{(2)}(x,0) = 0 \quad \text{and} \quad \frac{\partial v_{\tau,\theta}^{(2)}}{\partial t}(x,0) = \delta\left(\frac{x \cdot \theta}{c_0} - \tau\right), \tag{1.9}$$

together with the boundary condition $v_{\tau,\theta}^{(2)} = 0$ on $\partial\Omega \setminus \Gamma \times (0,T)$.

Note that if $T \geq \frac{\operatorname{diam}(\Omega)}{c_0}$ in the full-view setting, our test functions $v_{\tau,\theta}^{(1)}$, $v_{\tau,\theta}^{(2)}$ and $w_{\tau,y}$ vanish at $t = T$. In the limited-view case, under the geometric controllability conditions [5] on Γ and T, existence of the test function v is guaranteed.

In both the full- and the limited-view cases, we get

$$\int_0^T \int_{\partial\Omega \text{ or } \Gamma} \frac{\partial p}{\partial \nu}(x,t)v_{\tau,\theta}^{(2)}(x,t)d\sigma(x)dt = \mathrm{R}[p_0](\theta,\tau), \tag{1.10}$$

where $\mathrm{R}[f]$ is the (line) Radon transform of f. Applying a classical filtered back-projection algorithm to the data (1.10), one can reconstruct $p_0(x)$.

To illustrate the need of this approach, we present in Figure 1.9 the reconstruction results from data with homogeneous Dirchlet boundary conditions. We compare the reconstruction using the inverse spherical Radon transform with the duality approach presented above. It appears that not taking boundary conditions into account leads to important errors in the reconstruction.
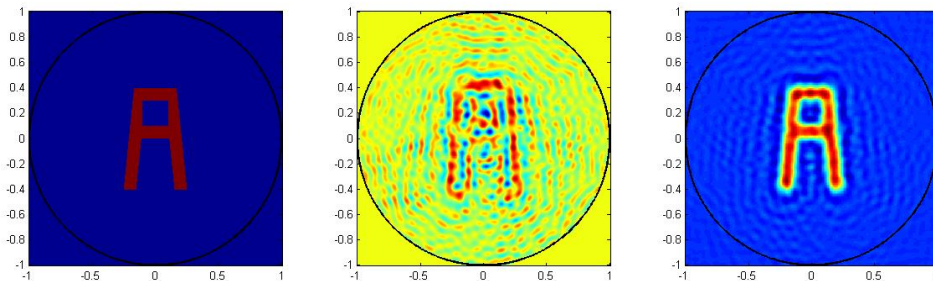

Fig. 1.9. Reconstruction in the case of homogeneous Dirichlet boundary conditions. Left: initial condition p_0; Center: reconstruction using spherical Radon transform; Right: reconstruction using probe functions algorithm.

We then tested this approach on the Shepp-Logan phantom, using the family of probe functions $v^{(2)}_{\tau,\theta}$. Reconstructions are given in Figure 1.10. We notice numerical noise due to the use of discontinuous (Heaviside) test functions against discrete measurements.

The numerical tests were conducted using Matlab. Three different forward solvers have been used for the wave equation:

- a FDTD solver, with Newmark scheme for time differentiation;
- a space-Fourier solver, with Crank-Nicholson finite difference scheme in time;
- a space-(P1) FEM-time finite difference solver.

Measurements were supposed to be obtained on equi-distributed captors on a circle or a square. The use of integral transforms (line or spherical Radon transform) avoids inverse crime since such transforms are computed on a different class of parameters (center and radius for spherical Radon transforms, direction and shift for line Radon transform). Indeed, their numerical inversions (achieved using formula (1.3) or the iradon function of Matlab) are not computed on the same grid as the one for the forward solvers.
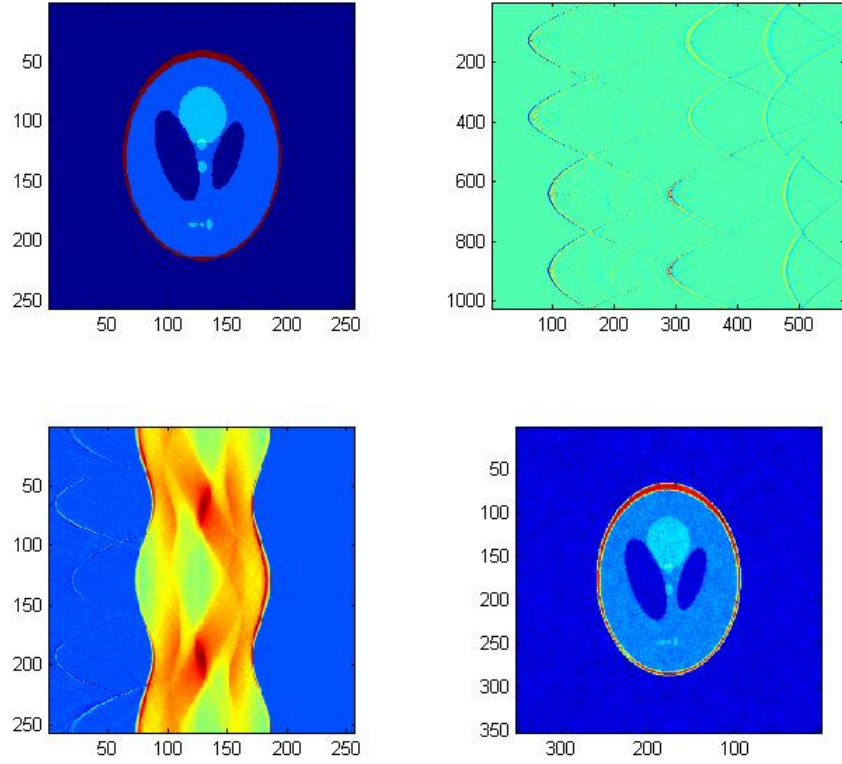
Fig. 1.10. Numerical inversion in the case of homogeneous Dirichlet boundary conditions. Here, $N = 256$, $N_R = 200$ and $N_\theta = 200$. Top left: p_0; Top right: $p(y,t)$ with $(y,t) \in \partial\Omega \times (0,3)$; Bottom left: $\mathcal{R}[p_0]$; Bottom right: reconstruction using probe functions algorithm.

1.3.3 Compensation of the effect of acoustic attenuation

Our aim in this section is to compensate the effect of acoustic attenuation. Let $p_a(x,t)$ be the solution of the wave equation in a dissipative medium:

$$\frac{1}{c_0^2}\frac{\partial^2 p_a}{\partial t^2}(x,t) - \Delta p_a(x,t) - L(t) * p_a(x,t) = \frac{1}{c_0^2}\delta'_{t=0}p_0(x) \qquad \text{in } \Omega \times \mathbb{R},$$

(1.11)

with the Dirichlet (resp. the Neumann) imposed boundary conditions:

$$p_a(x,t) = 0 \qquad \left(\text{resp. } \frac{\partial p_a}{\partial \nu}(x,t) = 0\right) \qquad \text{on } \partial\Omega \times \mathbb{R}, \qquad (1.12)$$

where L is defined by (1.6).

We want to recover $p_0(x)$ from boundary measurements of $\dfrac{\partial p_a}{\partial \nu}(x,t)$ (resp. $p_a(x,t)$). Again, we assume that a is small.

Taking the Fourier transform of (1.11) yields

$$
\begin{cases}
(\Delta + K^2(\omega))\hat{p}_a(x,\omega) = \dfrac{i\omega}{\sqrt{2\pi}c_0^2}p_0(x) & \text{in } \Omega, \\[2mm]
\hat{p}_a(x,\omega) = 0 \qquad \left(\text{resp. } \dfrac{\partial \hat{p}_a}{\partial \nu}(x,\omega) = 0\right) & \text{on } \partial\Omega,
\end{cases}
\tag{1.13}
$$

where $\hat{p}_a$ denotes the Fourier transform of p_a.

1.3.4 Case of a spherical wave as a probe function

By multiplying (1.13) by the Fourier transform, $\hat{w}_{0,y}(x,\omega)$, of $w_{\tau=0,y}$ given by (1.6), we arrive at, for any τ,

$$
\frac{i}{\sqrt{2\pi}} \int_\Omega p_0(x)\left(\int_\mathbb{R} \omega e^{i\omega\tau}\hat{w}_{0,y}(x,K(\omega))\,d\omega\right) dx = \int_\mathbb{R} e^{i\omega\tau} \int_{\partial\Omega} \frac{\partial\hat{p}_a}{\partial\nu}(x,\omega)\hat{w}_{0,y}(x,K(\omega))\,d\omega,
\tag{1.14}
$$

for the Dirichlet problem and

$$
\frac{i}{\sqrt{2\pi}} \int_\Omega p_0(x)\left(\int_\mathbb{R} \omega e^{i\omega\tau}\hat{w}_{0,y}(x,K(\omega))\,d\omega\right) dx = -\int_\mathbb{R} e^{i\omega\tau} \int_{\partial\Omega} \hat{p}_a(x,\omega)\frac{\partial\hat{w}_{0,y}}{\partial\nu}(x,K(\omega))\,d\omega,
\tag{1.15}
$$

for the Neumann problem.

Next we compute $\int_\mathbb{R} \omega e^{i\omega\tau}\hat{w}_{0,y}(x,K(\omega))\,d\omega$ for the thermo-viscous model. Recall that in this case,

$$
K(\omega) \approx \frac{\omega}{c_0} + \frac{ia\omega^2}{2}.
$$

We have

$$
\int_\mathbb{R} \omega e^{i\omega\tau}\hat{w}_{0,y}(x,K(\omega))\,d\omega \approx \frac{1}{4\pi|x-y|}\int_\mathbb{R} \omega e^{i\omega(\tau - \frac{|x-y|}{c_0})}e^{-a\omega^2\frac{|x-y|}{c_0}}\,d\omega, \tag{1.16}
$$

and again, the stationary phase theorem can then be applied to approximate the inversion procedure for $p_0(x)$.

Note that if we use the Fourier transform $\hat{v}$ of (1.5) or (1.8) as a test function then we have to truncate the integral in (1.14) since $\hat{v}(x,K(\omega))$ is exponentially growing in some regions of Ω.

1.3.5 Case of a plane wave as a probe function

Let us first introduce the function $\tilde{K}(\omega)$ defined by $\tilde{K}(\omega) = \sqrt{\overline{K(\omega)^2}}$ and consider a solution of the Helmholtz equation

$$\left(\Delta + \tilde{K}^2(\omega) \right) \hat{v}_a(x, \omega) = 0$$

of the form

$$\hat{v}_a(x, \omega) = e^{-i\omega(x \cdot \theta - c_0 \tau)} g(\omega), \tag{1.17}$$

where $g(\omega)$ decays sufficiently fast.

Multiplying (1.13) by $\hat{v}_a(x, \omega)$, we obtain

$$\frac{i}{\sqrt{2\pi}} \int_\Omega p_0(x) \left(\int_{\mathbb{R}} \omega \overline{\hat{v}_a(x, \omega)} d\omega \right) dx = \int_{\mathbb{R}} \int_{\partial\Omega} \frac{\partial \hat{p}_a}{\partial \nu}(x, \omega) \overline{\hat{v}_a(x, \omega)} d\sigma(x) d\omega. \tag{1.18}$$

Since $\tilde{K}(\omega) \simeq \frac{\omega}{c_0} - \frac{ia\omega^2}{2}$, then by taking in formula (1.17)

$$g(\omega) = e^{-\frac{1}{2}\omega^2 ac_0 T} \quad \text{and} \quad g(\omega) = \frac{1}{i\omega} e^{-\frac{1}{2}\omega^2 ac_0 T},$$

we can use the plane waves $\hat{v}_a^{(1)}$ and $\hat{v}_a^{(2)}$ given by

$$\hat{v}_a^{(1)}(x, \omega) = e^{-i\omega(x \cdot \theta - c_0 \tau)} e^{-\frac{1}{2}\omega^2 ac_0 (T + \frac{x \cdot \theta}{c_0} - \tau)},$$

and

$$\hat{v}_a^{(2)}(x, \omega) = \frac{1}{i\omega} e^{-i\omega(x \cdot \theta - c_0 \tau)} e^{-\frac{1}{2}\omega^2 ac_0 (T + \frac{x \cdot \theta}{c_0} - \tau)},$$

as approximate probe functions.

Take T sufficiently large such that $\left(T + \frac{x \cdot \theta}{c_0} - \tau \right)$ stays positive for all $x \in \Omega$. Thus,

$$v_a^{(1)}(x, t) \simeq \frac{1}{\sqrt{ac_0 \left(T + \frac{x \cdot \theta}{c_0} - \tau \right)}} e^{-\frac{(x \cdot \theta - c_0 \tau + t)^2}{2ac_0 \left(T + \frac{x \cdot \theta}{c_0} - \tau \right)}},$$

and

$$v_a^{(2)}(x, t) \simeq \mathrm{erf}\left(\frac{x \cdot \theta - c_0 \tau + t}{\sqrt{ac_0 \left(T + \frac{x \cdot \theta}{c_0} - \tau \right)}} \right).$$

Now using $v_a^{(2)}$ in formula (1.18) leads to the convolution of the Radon transform of p_0 with a quasi-Gaussian kernel. Indeed, the left hand-side of (1.18) satisfies

$$\frac{i}{\sqrt{2\pi}} \int_\Omega p_0(x) \left(\int_\mathbb{R} \overline{\omega \hat{v}_a^{(2)}(x,w))} d\omega \right) dx$$

$$\simeq \int_\Omega p_0(x) \frac{1}{\sqrt{ac_0 \left(T + \frac{x\cdot\theta}{c_0} - \tau \right)}} e^{-\frac{(x\cdot\theta - c_0\tau)^2}{2ac_0 \left(T + \frac{x\cdot\theta}{c_0} - \tau \right)}} dx$$

$$= \int_{s_{\min}}^{s_{\max}} R[p_0](\theta, s) \frac{1}{\sqrt{ac_0 \left(T + \frac{s}{c_0} - \tau \right)}} e^{-\frac{(s - c_0\tau)^2}{2ac_0 \left(T + \frac{s}{c_0} - \tau \right)}} ds,$$

and the right hand-side is explicitly estimated by

$$\int_\mathbb{R} \int_{\partial\Omega} \frac{\partial \hat{p}_a}{\partial \nu}(x,\omega) \overline{\hat{v}_a^{(2)}(x,\omega)} d\sigma(x) d\omega \simeq \int_0^T \int_{\partial\Omega} \frac{\partial p_a}{\partial \nu}(x,t) \mathrm{erf}\left(\frac{x\cdot\theta - c_0\tau + t}{\sqrt{ac_0 \left(T + \frac{x\cdot\theta}{c_0} - \tau \right)}} \right) d\sigma(x) dt.$$

As previously, we can compensate the effect of attenuation using the stationary phase theorem for the operator $\tilde{\mathcal{L}}$,

$$\tilde{\mathcal{L}}[\phi](\tau) = \int_{s_{\min}}^{s_{\max}} \phi(s) \frac{1}{\sqrt{ac_0 \left(T + \frac{s}{c_0} - \tau \right)}} e^{-\frac{(s - c_0\tau)^2}{2ac_0 \left(T + \frac{s}{c_0} - \tau \right)}} ds,$$

which reads

$$\tilde{\mathcal{L}}[\phi](\tau) \simeq \phi(c_0\tau) + \frac{ac_0 T}{2} \left(\phi''(c_0\tau) + \frac{2\phi'(c_0\tau)}{c_0 T} \right). \tag{1.19}$$

See appendix A.3. More generally,

$$\tilde{\mathcal{L}}[\phi](\tau) = \sum_{i=0}^k \frac{(c_0 a)^i}{2^i i!} D_i[\phi] + o(a^k), \tag{1.20}$$

where the differential operators D_i satisfy

$$D_i[\phi] = ((T + \frac{s}{c_0} - \tau)^i [\phi](s))_{|s=c_0\tau}^{(2i)}.$$

Define $\tilde{\mathcal{L}}_k^{-1}$ as in (1.11). Using (1.20), we reconstructed the line Radon transform of p_0 correcting the effect of attenuation. We then applied a standard filtered back-projection algorithm to inverse the Radon transform. Results are given in Figure 1.11.
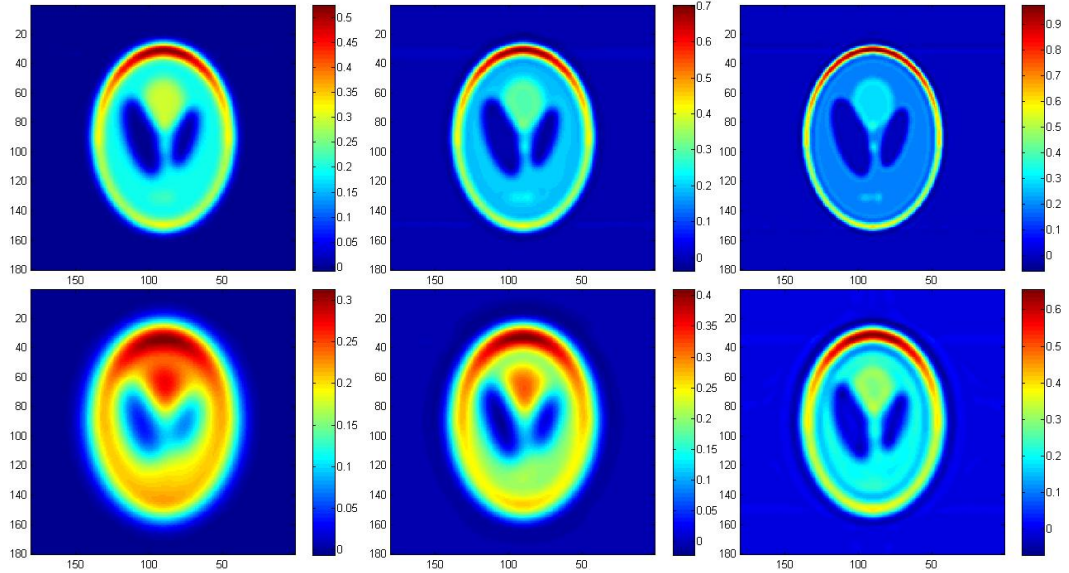
Fig. 1.11. Compensation of acoustic attenuation with formula (1.19) in the case of homogeneous Dirichlet boundary conditions. Here, $N = 256$, $N_R = 200$ and $N_\theta = 200$. First line: $a = 0.0005$; Second line: $a = 0.0025$. Left: $\tilde{\mathcal{L}}_k^{-1}$ with $k = 0$; Center: $\tilde{\mathcal{L}}_k^{-1}$ with $k = 1$; Right: $\tilde{\mathcal{L}}_k^{-1}$ with $k = 8$.

1.4 Conclusion

In this chapter we have provided new approaches to correct the effect of imposed boundary conditions as well as the effect of acoustic attenuation.

It would be very interesting to analytically investigate their robustness with respect to measurement noise and medium noise. In this connection, we refer to [4] for a coherent interferometric strategy for photo-acoustic imaging in the presence of microscopic random fluctuations of the speed of sound.

Another important problem is to *a priori* estimate the attenuation coefficient a and the frequency power ζ.

Finally, it is worth emphasizing that it is the absorption coefficient, not the absorbed energy, that is a fundamental physiological parameter. The absorbed energy density is in fact the product of the optical absorption coefficient and the light fluence which depends on the distribution of scattering and absorption within the domain, as well as the light sources. In [3], methods for reconstructing the normalized optical absorption coefficient of small absorbers from the absorbed density are proposed. Multi-wavelength acoustic measurements are combined with diffusing light measurements to separate the product of absorption coefficient and optical fluence. In the case of extended absorbers, multi-wavelength photo-acoustic imaging is also expected to lead to a satisfactory solution [11].

A Stationary phase theorem and proofs of (1.10) and (1.19)

A.1 Stationary phase theorem

Theorem A.1 (Stationary Phase [18]) *Let $K \subset [0, \infty)$ be a compact set, X an open neighborhood of K and k a positive integer. If $\psi \in \mathcal{C}_0^{2k}(K)$, $f \in \mathcal{C}^{3k+1}(X)$ and $Im(f) \geq 0$ in X, $Im(f(t_0)) = 0$, $f'(t_0) = 0$, $f''(t_0) \neq 0$, $f' \neq 0$ in $K \setminus \{t_0\}$ then for $\epsilon > 0$*

$$\left| \int_K \psi(t) e^{if(t)/\epsilon} dt - e^{if(t_0)/\epsilon} \left(\epsilon^{-1} f''(t_0)/2\pi i \right)^{-1/2} \sum_{j<k} \epsilon^j L_j[\psi] \right| \leq C\epsilon^k \sum_{\alpha \leq 2k} \sup |\psi^{(\alpha)}(x)|.$$

Here C is bounded when f stays in a bounded set in $\mathcal{C}^{3k+1}(X)$ and $|t - t_0|/|f'(t)|$ has a uniform bound. With,

$$g_{t_0}(t) = f(t) - f(t_0) - \frac{1}{2} f''(t_0)(t - t_0)^2,$$

which vanishes up to third order at t_0, and

$$L_j[\psi] = \sum_{\nu - \mu = j} \sum_{2\nu \geq 3\mu} i^{-j} \frac{2^{-\nu}}{\nu! \mu!} (-1)^\nu f''(t_0)^{-\nu} (g_{t_0}^\mu \psi)^{(2\nu)}(t_0).$$

We will use this theorem with $k = 2$. Note that L_1 can be expressed as the sum $L_1[\psi] = L_1^{(1)}[\psi] + L_1^{(2)}[\psi] + L_1^{(3)}[\psi]$, where $L_1^{(j)}$ is respectively associated to the couple $(\nu_j, \mu_j) = (1, 0), (2, 1), (3, 2)$ and is identified as

$$\begin{cases} L_1^{(1)}[\psi] & = -\frac{1}{2i} f''(t_0)^{-1} \psi^{(2)}(t_0), \\ L_1^{(2)}[\psi] & = \frac{1}{2^2 2! i} f''(t_0)^{-2} (g_{t_0}\psi)^{(4)}(t_0) = \frac{1}{8i} f''(t_0)^{-2} \left(g_{t_0}^{(4)}(t_0)\psi(t_0) + 4g_{t_0}^{(3)}(t_0)\psi'(t_0) \right), \\ L_1^{(3)}[\psi] & = \frac{-1}{2^3 2! 3! i} f''(t_0)^{-3} (g_{t_0}^2 \psi)^{(6)}(t_0) = \frac{-1}{2^3 2! 3! i} f''(t_0)^{-3} (g_{t_0}^2)^{(6)}(t_0)\psi(t_0). \end{cases}$$

A.2 Proof of approximation (1.10)

Let us now apply the stationary phase theorem to the operator $\tilde{\mathcal{L}}$

$$\tilde{\mathcal{L}}[\phi] = \frac{1}{\sqrt{2\pi}} \int_0^{+\infty} \phi(t) \frac{1}{\sqrt{c_0 a t}} e^{-\frac{1}{2} \frac{(s-t)^2}{c_0 a t}} dt.$$

Note that the integral

$$J(s) = \int_0^\infty \psi(t) e^{if(t)/\epsilon} dt,$$

24   H. Ammari et al.

with $\psi(t) = \frac{\phi(t)}{\sqrt{t}}$, $\epsilon = c_0 a$, $f(t) = i\frac{(t-s)^2}{2t}$, satisfies $J(s) = \sqrt{c_0 a 2\pi}\tilde{\mathcal{L}}[\phi]$. The phase f vanishes at $t = s$ and satisfies

$$f'(t) = i\frac{1}{2}\left(1 - \frac{s^2}{t^2}\right), \quad f''(t) = i\frac{s^2}{t^3}, \quad f''(s) = i\frac{1}{s}.$$

The function $g_s(t)$ is given by

$$g_s(t) = i\frac{1}{2}\frac{(t-s)^2}{t} - i\frac{1}{2}\frac{(t-s)^2}{s} = i\frac{1}{2}\frac{(s-t)^3}{ts}.$$

We can deduce that

$$\begin{cases} (g_s\psi)^{(4)}(s) = \left(g_{x_0}^{(4)}(s)\psi(s) + 4g_{x_0}^{(3)}(s)\psi'(s)\right) = i\frac{1}{2}\left(\frac{24}{s^3}\psi(s) - \frac{24}{s^2}\psi'(s)\right), \\ (g_s^2\psi)^{(6)}(s) = (g_{x_0}^2)^{(6)}(s)\psi(s) = -\frac{1}{4}\frac{6!}{s^4}\psi(s), \end{cases}$$

and then, with the same notation as in Theorem A.1,

$$\begin{cases} L_1^{(1)}[\psi] = -\frac{1}{i}\left(\frac{1}{2}(f''(s))^{-1}\psi''(s)\right) = \frac{1}{2}s\left(\frac{\phi}{\sqrt{s}}\right)'' = \frac{1}{2}\left(\sqrt{s}\phi''(s) - \frac{\phi'(s)}{\sqrt{s}} + \frac{3}{4}\frac{\phi}{s^{3/2}}\right), \\ L_1^{(2)}[\psi] = \frac{1}{8i}f''(s)^{-2}\left(g_s^{(4)}(s)\psi(s) + 4g_s^{(3)}(s)\psi'(s)\right) = \frac{1}{2}\left(3\left(\frac{\phi(s)}{\sqrt{s}}\right)' - 3\frac{\phi(s)}{s^{3/2}}\right) \\ \qquad = \frac{1}{2}\left(3\frac{\phi'(s)}{\sqrt{s}} - \frac{9}{2}\frac{\phi(s)}{s^{3/2}}\right), \\ L_1^{(3)}[\psi] = \frac{-1}{2^3 2! 3! i}f''(s)^{-3}(g_s^2)^{(6)}(s)\psi(s) = \frac{1}{2}\left(\frac{15}{4}\frac{\phi(s)}{s^{3/2}}\right). \end{cases}$$

The operator L_1 is given by

$$L_1[\psi] = L_1^{(1)}[\psi] + L_1^{(2)}[\psi] + L_1^{(3)}[\psi]$$
$$= \frac{1}{2}\left(\sqrt{s}\phi''(s) + (3-1)\frac{\phi'(s)}{\sqrt{s}} + \left(\frac{3}{4} - \frac{9}{2} + \frac{15}{4}\right)\frac{\phi(s)}{s^{3/2}}\right) = \frac{1}{2\sqrt{s}}(s\phi(s))'',$$

and so,

$$\left|J(s) - \sqrt{2\pi a c_0 s}\left(\frac{\phi(s)}{\sqrt{s}} + a\frac{1}{2\sqrt{s}}(s\phi(s))''\right)\right| \le Ca^2\sum_{\alpha \le 4}\sup|\phi^{(\alpha)}(x)|.$$

Finally, we arrive at

$$\left|\frac{1}{\sqrt{2\pi}}\int_0^\infty \phi(t)\frac{1}{\sqrt{ac_0 t}}e^{-\frac{(t-s)^2}{2ac_0 t}}dt - \left(\phi(s) + \frac{a}{2}(s\phi(s))''\right)\right| \le Ca^{3/2}\sum_{\alpha \le 4}\sup|\phi^{(\alpha)}(t)|.$$

A.3 Proof of approximation (1.19)

Let us now apply the stationary phase theorem to the operator $\mathcal{L}$ defined by

$$\tilde{\mathcal{L}}[\phi](\tau) = \frac{1}{\sqrt{2\pi}} \int_{s_{\min}}^{s_{\max}} \left[\phi(s) \left(a \left(c_0 T + s - c_0 \tau \right) \right)^{-\frac{1}{2}} e^{-\frac{(s - c_0 \tau)^2}{2a(c_0 T + s - c_0 \tau)}} \right] ds$$

$$= \frac{1}{\sqrt{2\pi}} \int_{s_{\min} - c_0 \tau}^{s_{\max} - c_0 \tau} \left[\phi(t + c_0 \tau) \left(a \left(\tilde{T} + t \right) \right)^{-\frac{1}{2}} e^{-\frac{t^2}{2a\left(\tilde{T} + t \right)}} \right] dt,$$

where $\tilde{T} = c_0 T$. Note that the integral

$$J(\tau) = \int_{s_{\min} - c_0 \tau}^{s_{\max} - c_0 \tau} \psi(t) e^{if(t)/\epsilon} dt,$$

with $\psi(t) = \frac{\phi(t + c_0 \tau)}{\sqrt{\tilde{T} + t}}$, $\epsilon = a$, $f(s) = i \frac{t^2}{2(\tilde{T} + t)}$, satisfies $J(\tau) = \sqrt{a 2\pi} \tilde{\mathcal{L}}[\phi]$.
The phase f vanishes at $t = 0$ and satisfies

$$f'(t) = i \frac{1}{2} \frac{t(t + 2\tilde{T})}{(t + \tilde{T})^2}, \quad f''(t) = i \frac{\tilde{T}^2}{(t + \tilde{T})^3}, \quad f''(0) = i \frac{1}{\tilde{T}}.$$

The function $g_0(t)$ is identified as

$$g_0(t) = -i \frac{1}{2} \frac{t^3}{\tilde{T}(\tilde{T} + t)}.$$

We have

$$\begin{cases} (g_0 \psi)^{(4)}(0) &= \left(g_0^{(4)}(0) \psi(0) + 4 g_0^{(3)}(0) \psi'(0) \right) = i \frac{1}{2} \left(\frac{24}{\tilde{T}^3} \psi(0) - \frac{24}{\tilde{T}^2} \psi'(0) \right), \\ (g_0^2 \psi)^{(6)}(0) &= (g_0^2)^{(6)}(0) \psi(0) = -\frac{1}{4} \frac{6!}{\tilde{T}^4} \psi(0), \end{cases}$$

and

$$\psi(0) = \frac{\phi(c_0 \tau)}{\tilde{T}^{1/2}}, \quad \psi'(0) = \frac{\phi'(c_0 \tau)}{\tilde{T}^{1/2}} - \frac{1}{2} \frac{\phi(c_0 \tau)}{\tilde{T}^{3/2}}, \quad \psi''(0) = \frac{\phi''(c_0 \tau)}{\tilde{T}^{1/2}} - \frac{\phi'(c_0 \tau)}{\tilde{T}^{3/2}} + \frac{3}{4} \frac{\phi(c_0 \tau)}{\tilde{T}^{5/2}}.$$

Therefore, again with the same notation as in Theorem A.1,

$$\begin{cases} L_1^{(1)}[\psi] = -\frac{1}{i} \left(\frac{1}{2} (f''(0))^{-1} \psi''(0) \right) = \frac{1}{2} \left(\sqrt{\tilde{T}} \phi''(c_0 \tau) - \frac{\phi'(c_0 \tau)}{\tilde{T}^{1/2}} + \frac{3}{4} \frac{\phi(c_0 \tau)}{\tilde{T}^{3/2}} \right), \\[2mm] L_1^{(2)}[\psi] = \frac{1}{8i} f''(0)^{-2} \left(g_0^{(4)}(0) \psi(0) + 4 g_0^{(3)}(0) \psi'(0) \right) = \frac{1}{2} \left(3 \psi'(0) - 3 \frac{\psi(0)}{\tilde{T}} \right) \\[2mm] \qquad = \frac{1}{2} \left(3 \frac{\phi'(c_0 \tau)}{\tilde{T}^{1/2}} - \frac{9}{2} \frac{\phi(c_0 \tau)}{\tilde{T}^{3/2}} \right), \\[2mm] L_1^{(3)}[\psi] = -\frac{1}{2^3 2! 3! i} f''(0)^{-3} (g_0^2)^{(6)}(0) \psi(0) = \frac{1}{2} \left(\frac{15}{4} \frac{\phi(c_0 \tau)}{\tilde{T}^{3/2}} \right), \end{cases}$$

and L_1 is given by

$$L_1[\psi] = L_1^{(1)}[\psi] + L_1^{(2)}[\psi] + L_1^{(3)}[\psi] = \frac{1}{2\sqrt{\tilde{T}}} \left(\tilde{T}\phi''(c_0\tau) + 2\phi'(c_0\tau) \right)$$

$$= \frac{1}{2\sqrt{\tilde{T}}} \left((s - c_0\tau + \tilde{T})\phi(s) \right)''_{\lfloor s=c_0\tau},$$

which yields

$$\left| J(\tau) - \sqrt{2\pi a} \left(\phi(c_0\tau) + a/2 \left((s - c_0\tau + c_0 T)\phi(s) \right)''_{\lfloor s=c_0\tau} \right) \right| \leq Ca^2 \sum_{\alpha \leq 4} \sup |\phi^{(\alpha)}(x)|.$$

Hence,

$$\left| \tilde{\mathcal{L}}[\phi] - \left(\phi(c_0\tau) + \frac{ac_0 T}{2} \left(\phi''(c_0\tau) + \frac{2\phi'(c_0\tau)}{c_0 T} \right) \right) \right| \leq Ca^{3/2} \sum_{\alpha \leq 4} \sup |\phi^{(\alpha)}(t)|.$$

References

1. H. Ammari, M. Asch, L. Guadarrama Bustos, V. Jugnon and H. Kang, Transient wave imaging with limited-view data, SIAM J. Imag. Sci, submitted.
2. H. Ammari, E. Bossy, V. Jugnon, and H. Kang, Mathematical modelling in photo-acoustic imaging of small absorbers, SIAM Rev., to appear.
3. H. Ammari, E. Bossy, V. Jugnon, and H. Kang, Quantitative photo-acoustic imaging of small absorbers, SIAM J. Appl. Math., submitted.
4. H. Ammari, J. Garnier, and V. Jugnon, Coherent interferometric strategy for photo-acoustic imaging, in this volume.
5. C. Bardos, G. Lebeau, and J. Rauch, Sharp sufficient conditions for the observation, control, and stabilization of waves from the boundary, SIAM J. Control Optim., 30 (1992), 1024-1065.
6. A. Beck and M. Teboulle, A fast iterative shrinkage-thresholding algorithm for linear inverse problems, SIAM J. Imaging Sci., 2 (2009), 183–202.
7. P. Burgholzer, H. Grün, M. Haltmeier, R. Nuster, and G. Paltauf, Compensation of acoustic attenuation for high resolution photoacoustic imaging with line detectors, Proc. of SPIE, 6437 (2007), 643724.
8. A. Chambolle, An algorithm for total variation minimization and applications, J. Math. Imag. Vis., 20 (2004), 89–97.
9. W. Chen and S. Holm, Fractional Laplacian time-space models for linear and nonlinear lossy media exhibiting arbitrary frequency power-law dependency, J. Acoust. Soc. Amer., 115 (2004), 1424–1430.
10. P. Combettes and V. Wajs, Signal recovery by proximal forward-backward splitting, Mult. Model. Simul., 4 (2005), 1168–1200.
11. B.T. Cox, J.G. Laufer, and P.C. Beard, The challenges for quantitative photoacoustic imaging, Proc. of SPIE, 7177 (2009), 717713.
12. I. Daubechies, M. Defrise and C. De Mol, An iterative thresholding algorithm for linear inverse problems with a sparsity constraint, Comm. Pure Appl. Math., 57 (2004), 1413–1457.

13. D. Finch, M. Haltmeier, and Rakesh, Inversion of spherical means and the wave equation in even dimensions, SIAM J Appl Math, 68 (2007), 392–412.
14. D. Finch, S. Patch, and Rakesh, Determining a function from its mean-values over a family of spheres, SIAM J. Math. Anal., 35 (2004), 1213–1240.
15. M. Haltmeier, R. Kowar, A. Leitao, and O. Scherzer, Kaczmarz methods for regularizing nonlinear ill-posed equations II: Applications, Inverse Problems and Imaging, 1 (2007), 507–523.
16. M. Haltmeier, T. Schuster, and O. Scherzer, Filtered backprojection for thermoacoustic computed tomography in spherical geometry, Math. Meth. Appl. Sci., 28 (2005), 1919-1937.
17. M. Haltmeier, O. Scherzer, P. Burgholzer, R. Nuster, and G. Paltauf, Thermoacoustic tomography and the circular Radon transform: exact inversion formula, Math. Model. Meth. Appl. Sci., 17(4) (2007), 635-655.
18. L. Hörmander, *The Analysis of Linear Partial Differential Operators. I. Distribution Theory and Fourier Analysis*, Classics in Mathematics, Springer-Verlag, Berlin, 2003.
19. R. Kowar, Integral equation models for thermoacoustic imaging of dissipative tissue, Inverse Problems, 26 (2010), 095005 (18pp).
20. R. Kowar and O. Scherzer, Photoacoustic imaging taking into account attenuation, in this volume.
21. R. Kowar, O. Scherzer, and X. Bonnefond, Causality analysis of frequency dependent wave attenuation, Math. Meth. Appl. Sci., to appear.
22. P. Kuchment and L. Kunyansky, Mathematics of photoacoustics and thermoacoustic tomography, in *Handbook of Mathematical Methods in Imaging* (ed: O. Scherzer), Springer-Verlag, New York, 2011.
23. P. Kunchment and L. Kunyansky, Mathematics of thermoacoustic tomography, Europ. J. Appl. Math., 19 (2008), 191–224.
24. L. Kunyansky, Explicit inversion formulas for the spherical mean Radon transform, Inverse Problems, 23 (2007), 373–383.
25. P.J. La Rivière, J. Zhang, and M.A. Anastasio, Image reconstruction in optoacoustic tomography for dispersive acoustic media, Opt. Lett., 31 (2006), 781–783.
26. K. Maslov, H. F. Zhang, and L. V. Wang, Effects of wavelength-dependent fluence attenuation on the noninvasive photoacoustic imaging of hemoglobin oxygen saturation in subcutaneous vasculature in vivo, Inverse Problems, 23 (2007), S113–S122.
27. L.V. Nguyen, A family of inversion formulas in thermoacoustic tomography, Inverse Problems and Imaging, 3 (2009), 649–675 .
28. K. Patch and M. Haltmeier, Thermoacoustic tomography - ultrasound attenuation artifacts, IEEE Nuclear Science Symposium Conference, 4 (2006), 2604–2606.
29. N.V. Sushilov and R.S.C. Cobbold, Frequency-domain wave equation and its time-domain solutions in attenuating media, J. Acoust. Soc. Am., 115 (2004), 1431–1436.
30. T. L. Szabo. Causal theories and data for acoustic attenuation obeying a frequency power law. *Journal of Acoustical Society of America*, 97 (1995), 14–24.
31. B.E. Treeby and B.T. Cox, Fast, tissue-realistic models of photoacoustic wave propagation for homogeneous attenuating media, Proc. of SPIE, 7177 (2009), 717716.

32. L.V. Wang and X. Yang, Boundary conditions in photoacoustic tomography and image reconstruction, J. Biomed. Optics, 12 (2007), 014027.
33. M. Xu and L.V. Wang, Photoacoustic imaging in biomedicine, Rev. Scient. Instrum., 77 (2006), 041101.
34. Y. Xu and L.V. Wang, Reconstructions in limited-view thermoacoustic tomography, Medical Physics, 31 (2004), 724–733.